# Unifying disparate rate-dependent rheological regimes in non-Brownian suspensions

R. V. More ● and A. M. Ardekani ●[*]

*School of Mechanical Engineering, Purdue University, West Lafayette, Indiana 47907, USA*

A typical dense non-Brownian particulate suspension exhibits shear thinning (decreasing viscosity) at low shear rate or stress followed by a Newtonian plateau (constant viscosity) at intermediate shear rate or stress values which transitions to shear thickening (increasing viscosity) beyond a critical shear rate or stress value and finally undergoes a second shear thinning transition at extremely high shear rate or stress values. In this study, we unify and quantitatively reproduce all the disparate rate-dependent regimes and the corresponding transitions for a dense non-Brownian suspension with increasing shear rate or stress. We employ discrete particle dynamics simulations based on the proposed mechanism to elucidate its accuracy. We find that a competition between interparticle interactions of hydrodynamic and nonhydrodynamic origins and the switching in the dominant stress scale with increasing the shear rate or stress lead to each of the above transitions. Inclusion of traditional hydrodynamic interactions, attractive or repulsive Derjaguin-Landau-Verwey-Overbeek (DLVO) interactions the interparticle contact interactions, and a constant friction (or other constraint mechanism) reproduces the initial thinning as well as the shear thickening transition. However, to quantitatively capture the intermediate Newtonian plateau and the second shear thinning, an additional nonhydrodynamic interaction of non-DLVO origin and a decreasing coefficient of friction, respectively, are essential, thus providing an explanation for the presence of the intermediate Newtonian plateau along with reproducing the second shear thinning in a single framework. Expressions utilized for various interactions and friction are determined from experimental measurements and hence result in excellent quantitative agreement between the simulations and previous experiments.

## I. INTRODUCTION

Dense suspensions of particles are abundant in nature and industrial applications with examples ranging from household cornstarch solution to metallic pastes used in solar cells [1]. In spite of the Newtonian behavior of the suspending fluid medium, suspensions exhibit a plethora of non-Newtonian behaviors including yield stress [2], nonzero normal stress differences [3], shear-rate-dependent rheology [4,5], and particle migration [6], to name a few [7]. The consensus among researchers is that there is no timescale but a stress scale that gives rise to the nonlinear rate-dependent behavior in dense particulate suspensions [8].

Historically, it has been reported that a typical dense (volume fraction, $\phi \gtrsim 0.5$) non-Brownian suspension [particle sizes greater than $O(1~\mu m)$] exhibits four distinct rate-dependent regimes in its rheological flow curve. The suspension's rheological behavior transitions from one regime to another with an increase in the imposed shear rate or stress. The suspension exhibits shear thinning (decreasing viscosity) at low shear rates followed by a Newtonian plateau (almost constant viscosity) at intermediate shear rates which transitions to shear thickening (ST) (increasing viscosity) beyond a critical shear rate. Shear thickening can be gradual [continuous ST (CST)] or sudden [discontinuous ST (DST)]. Finally, if we further increase the shear rate or stress to extremely high

values, the suspension again undergoes another shear thinning transition [4,5,7,9,10]. This is depicted in Fig. 1.

Numerical models and theoretical studies to date are able to quantitatively capture the shear thinning at low shear rates [2,11,12] and the ST transition at intermediate shear rates [11–16]. The initial shear thinning at low shear rates arises from the presence of a repulsive double layer barrier (steric interactions) and the van der Waals attractive forces [collectively known as Derjaguin-Landau-Verwey-Overbeek (DLVO) interactions].
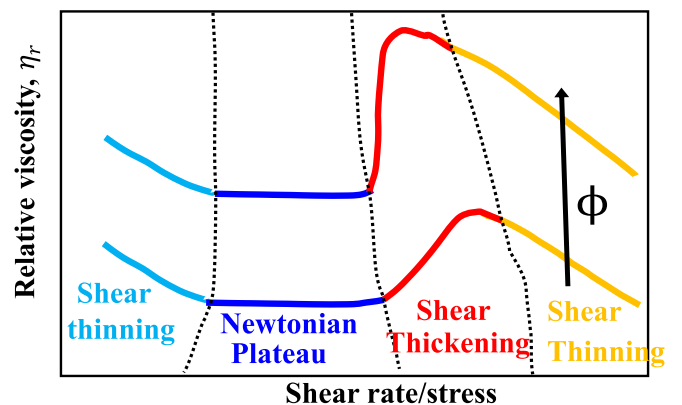


FIG. 1. Schematic showing the typical rheological flow curve for dense non-Brownian suspensions. This rheological behavior is commonly observed for non-Brownian suspensions [4,5,7,9].

---

*ardekani@purdue.edu

Shear thickening in suspensions has been known from the early 20th century and has been an active topic of research since then. As a result, a plethora of explanations for this phenomenon can be found in the literature. Some of these explanations include the sudden emergence of turbulence between the particles [17], order-disorder transitions [18,19], and hydrodynamics-induced particle clustering [13,20–22], but none of these explanations can quantitatively reproduce the viscosity jump observed in ST transitions [11,23,24]. For example, purely hydrodynamic-interaction-based simulations [14,25–27] give a weak logarithmic shear thickening (weak CST). Even though this purely hydrodynamics-based point of view is able to describe the rheology of moderately concentrated suspensions ($\phi < 45\%$) which exhibit a weak CST, it cannot predict the strong CST and CST to DST transition routinely observed in highly concentrated suspensions ($\phi > 50\%$) [11,22,28–31]. The recently proposed lubricated to frictional transition of the particle contacts [11,32,33] and constraint-based mechanisms [12,34] have been proven to be very efficient in capturing the ST onset, the CST to DST transition, and the shear jamming in dense suspensions.

Over the years, many explanations have been given for the second shear thinning at extremely high shear rates. These include an increase in the maximum packing density due to breakdown of spanning clusters [35], elastohydrodynamic effects [36], microscale non-Newtonian shear thinning effects of the interstitial solvent [37], inhomogeneous microstructure at high shear rates after the ST transition [38], surface tension effects and eventual sample ejection [28], and adhesion-based constraint relaxation due to stress [12]. However, none of these explanations can make quantitative predictions for the second shear thinning regime. In addition, the reason for the intermediate Newtonian plateau still eludes researchers [5,7], thus limiting the existing numerical and theoretical frameworks from being able to quantitatively reproduce the entire unified flow curve. Hence, understanding the origins of the Newtonian plateau is a crucial piece of the puzzle that allows us to unify all four rate-dependent regimes and the corresponding transitions from one regime to another.

To this end, we propose a unifying mechanism which quantitatively reproduces various regimes and transitions in the rheological flow curve of a dense non-Brownian suspension of smooth hard spheres. Since we are specifically interested in non-Brownian suspensions, we assume the Péclet number Pe to be much greater than $O(10^3)$, which typically corresponds to particle sizes greater than $O(1\ \mu\mathrm{m})$. Quantitative agreement between the discrete particle dynamics simulations based on the proposed mechanism and the experimental data bolsters the validity of the proposed model. Though pieces of this puzzle have been studied in detail in the context of specific suspensions showing specific behaviors, e.g., initial shear thinning due to the presence of attractive forces [2] and ST due to the lubricated to frictional contact transition [11,30,39], here we put forth an effort to unify all four disparate regimes. Furthermore, as mentioned, there is no explanation for the Newtonian plateau in the literature and the explanations given for the second shear thinning are not quantitative. We show that the inclusion of interparticle interactions of non-DLVO origin is the key to explaining and quantitatively capturing the intermediate Newtonian plateau regime. Relaxation of con-

straint on the particle motion in the form of decreasing friction accurately predicts the second shear thinning, thus unifying all four disparate regimes observed in the flow curve of a non-Brownian dense suspension. Finally, we will also demonstrate the versatility of the proposed model to reproduce various other rheological flow curves containing one or more of the four above-mentioned regimes.

## II. PHILOSOPHY BEHIND UNIFICATION

In a Stokes flow regime, i.e., where the particle Reynolds number Re is negligible, the particle motion in suspensions is governed by a simple balance between the hydrodynamic ($\mathbf{F}^H$) and the sum of all other nonhydrodynamic interactions acting on the particle ($\sum_\alpha \mathbf{F}^\alpha$) [25]. Each of these interactions leads to corresponding stress scales in the system which scale as approximately $O(|\mathbf{F}^\alpha|/6\pi a^2)$, where $a$ is the particle characteristic length scale. This scaling implicitly tells us that each interaction is competing with the hydrodynamic interactions which scale as $|\mathbf{F}^H| \approx 6\pi \eta_0 a^2 \dot{\gamma}$, where $\dot{\gamma}$ is the imposed shear rate and $\eta_0$ is the suspending fluid viscosity. There is a consensus that the competition between these stress scales gives rise to the rate-dependent rheological behavior in dense suspensions [8]. Previous experiments [5] and computations [2] show that the attractive and repulsive forces of DLVO origin give rise to the first shear thinning at low shear rate suspensions and hence are the choice of interactions for capturing the first shear thinning regime. The exact expressions for DLVO interactions are readily available from theoretical analyses and previous experimental data [5,40].

We hypothesize that the presence of non-DLVO forces, which are noncontact interparticle interactions and become dominant when the particles are extremely close but not touching each other, delays the ST transition to higher shear rates after the initial shear thinning. This happens because non-DLVO forces introduce an additional stress scale which needs to be overcome before the activation of the constraint mechanism (explained below) required for ST transition and hence gives rise to the intermediate Newtonian plateau. The presence of the non-DLVO forces has been confirmed by experimental measurements [41] and has been analyzed theoretically as well [42–44]. The non-DLVO forces can arise due to the presence of charge layers on the particle surface or due to hydration effects [41]. As will be shown from the simulation results, it is the magnitude of the non-DLVO forces which determines the range of shear rate or stress where the Newtonian plateau is observed. The absence of non-DLVO interactions leads to the disappearance of the intermediate Newtonian plateau. The quantitative matching with the experimental data can only be obtained by accounting for the non-DLVO forces, thus corroborating the validity of this hypothesis.

Any microscopic mechanism that introduces constraints on particle motion can result in the shear thickening transition, while relaxation of such a constraint can qualitatively reproduce the shear thinning. Lubrication interactions between individual asperities on particle surfaces can lead to CST as well as DST [16]. Constraint formation and relaxation by stress e.g., adhesion, can qualitatively reproduce the shear thickening and shear thinning transitions,

respectively [12]. However, to obtain a quantitative matching with experiments, we must know the exact expressions from experimental measurements for these constraint interactions. Hard particle-particle contacts resulting in friction are a constraining mechanism which has been investigated thoroughly and hence exact expressions from experimental measurements are available. So, without the loss of generality, friction is the choice of constraint mechanism for this study to quantitatively reproduce the CST, DST, and CST to DST transition with increasing $\phi$ and second shear thinning in the flow curve of a dense non-Brownian suspension.

It has been shown that a sudden activation of friction between the particles as they come into dry contact owing to the irregularities on particle surfaces results in the ST transition (CST and DST depending on the suspensions volume fraction $\phi$) [11,45]. The same has also been validated by experiments [33,46]. This is analogous to activating a constraint on the relative motion between the particles. On the other hand, a coefficient of friction $\mu$ decreasing with the normal load between the particles is analogous to relaxation of the constraint and hence would result in shear thinning [1,47]. Constraint mechanisms based on friction have been proven to be very efficacious in reproducing various shear stress–shear rate curves that are observed experimentally for dense suspensions, CST to DST transition beyond a critical volume fraction, and most importantly jamming [48,49]. Furthermore, there are many experimental studies that validate the role of friction [33,46,47]. Hence, friction is the constraining mechanism utilized here. We would like to emphasize that, owing to the additive nature of the nonhydrodynamic forces, any other constraining mechanism can be readily used, given expressions for the interactions are known. So the proposed unifying mechanism utilizes the well known Stribeck curve for interparticle friction along with hydrodynamic, DLVO (attractive or repulsive forces), non-DLVO, and contact forces to unify disparate regimes in the flow curve of non-Brownian dense suspensions.

### A. Stribeck curve for friction

The Stribeck curve for friction has been used widely in the literature to explain the sliding phenomenon occurring in lubricated contacts [50]. In a typical Stribeck curve, the coefficient of friction $\mu$ is plotted as a function of the Sommerfeld number $S = \eta V / W$, where $\eta$ is the lubricant dynamic viscosity, $V$ is the relative sliding velocity between contacting surfaces, and $W$ is the normal load [50]. However, for rough surfaces, the surface asperity height dictates the full-film to boundary lubrication contact transition (see [51] and the references therein). Particle surface roughness is one of the important parameters governing the rheology of dense suspensions as even the most idealized smooth particles have surface irregularities of $O(0.001–0.01)$ times the particle radii [47]. These surface asperities not only lead to interparticle contacts, but also dictate the friction in interesting ways. Hence, efforts to investigate the influence of particle roughness on dense suspension rheology have gained much traction in recent years [16,45,49,52].

In the case of particles coming into contact, the average roughness height results in an additional secondary

length scale (along with the primary length scale, which is particle size $a$) in the system. While the particle-size distribution governs the hydrodynamic interactions, the secondary length scale introduces geometrical and interparticle force constraints [45]. So we define $\lambda$ as the dimensionless gap between the particles, i.e., $\lambda = h/h_r$. Here $h$ is the interparticle gap and $h_r$ is the average roughness height (defined below). High $\lambda$ ($\lambda > 2$) signifies well separated particle without a dry contact and the friction force is mostly due to lubrication interactions (full-film contact) [50]. The effect of increasing the shear rate or stress in the suspension is to reduce the average interparticle gap, thus bringing particles close to each other. As particles move closer to each other $\lambda$ decreases, and partial elastohydrodynamic lubrication (EHL) results in a sudden rise in $\mu$ [53,54]. In this regime ($1 < \lambda < 2$), partial dry contact between the particles is expected to occur. In addition, as the interparticle gap becomes comparable to the mean particle surface roughness size, repulsive forces of non-DLVO origin (arising due to hydration or a stagnant charge layer on the particle surface) are expected to be present with magnitudes a few orders higher than the repulsive forces of DLVO origin, viz., arising from the double layer potential [55–57].

As $\lambda$ decreases further ($\lambda < 1$), the contact enters boundary lubrication, i.e., full dry contact between the particles. In this regime, the coefficient of friction has a high value if the contact between the particles is elastic, which is true if the asperity deformation is smaller than a threshold value $\delta_c$ [58]. If $\lambda$ decreases even further, the contact enters a plastic regime, which results in a significant reduction in the coefficient of friction [58]. This reduction in the friction coefficient with plastic deformation of asperities requires a tremendous normal load, which happens only at extremely high shear rate or stress values. As a result, we get the second shear thinning regime. These phenomena are depicted in Fig. 2.

### B. Summary of relevant interactions

The transitions in the flow curves are governed by the competition between various stress scales in the system for non-Brownian suspensions. In the present study, we have four such stress scales that determine the various transitions.

(i) In the regime of attractive and repulsive forces when the particles are not touching and are separated, i.e., $\lambda > 2$ (full-film regime in the Stribeck curve), the friction is due to the tangential lubrication forces which is implicit in our hydrodynamic force modeling. Hence, Coulomb's friction law is not applicable.

(ii) The non-DLVO force is a noncontact force, and hence does not lead to constraints on sliding motion. This force is present only when the particles are not touching but are very close to each other, i.e., $1 < \lambda < 2$ (EHL regime on the Stribeck curve).

(iii) The interparticle contact and a high coefficient of friction when the particles just come into contact ($0.95 < \lambda \leqslant 1$) lead to the shear thickening transition.

(iv) The decrease in the coefficient of friction as the asperities deform more and enter a plastic region ($\lambda \leqslant 0.95$) explains the second shear thinning regime. It should be noted that the second shear thinning was also observed for nonat-
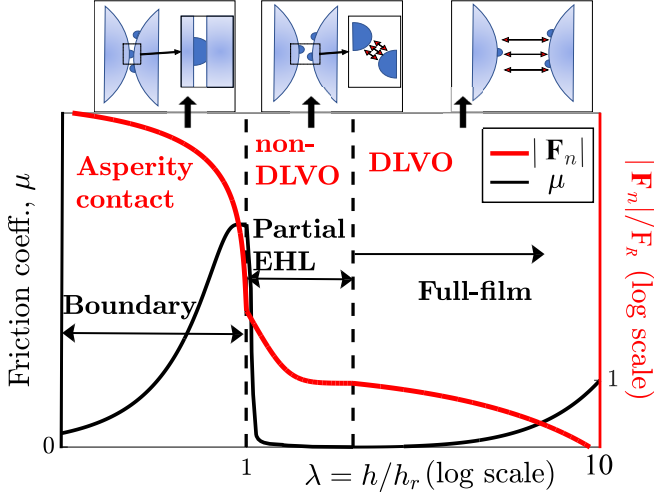
FIG. 2. Schematic showing the coefficient of friction $\mu$ (thin black line) and the dimensionless normal force magnitude $|\mathbf{F}_n|$ (thick red line) between a close particle pair as a function of dimensionless interparticle gap $\lambda = h/h_r$. Boundary, partial elastohydrodynamic, and full film lubrication regimes in the Stribeck curve are demarcated based on the value of $\lambda$. Similarly, dominant interparticle interactions in each of these regimes are also shown in red font. The insets at the top show the various regimes in terms of separation between two close particles. The arrows in these insets are shown to qualitatively indicate the size of the interparticle gap and the range of the dominant interparticle interaction with respect to the roughness and the particle size.

tractive and nonadhesive particles [10], which cannot be explained by stress-induced relaxation of constraints.

We briefly elaborate on the methods and simulation framework used in this study in the following section before presenting the main results.

## III. SIMULATION METHODOLOGY

We simulate the shear flow of neutrally buoyant inertialess bispherical particles with a radius ratio of 1.4 and equal volume fractions in a cubical domain of size $L = 15a$. Here $a$ is the radius of the smaller particle. For this particular particle-size distribution, the dry close packing fraction $\phi_d$ is 0.66 [49]. We use $\phi_d$ to normalize the volume fraction $\phi$ values in this study for direct comparison with experiments. Simulation results do not change much for a bigger domain size $L = 20a$. The suspending fluid is Newtonian with viscosity $\eta_0$. The imposed shear rate is $\dot{\gamma}$ with Lees-Edwards periodic boundary conditions on all sides. Also, the Péclet number $\text{Pe} > O(10^3)$ [4,5,7], so the flow is in the non-Brownian regime.

We use Ball-Melrose approximation [59] to calculate the hydrodynamic interactions $\mathbf{F}^H$, repulsive force of electrostatic origin $\mathbf{F}^R$, van der Waals attractive force $\mathbf{F}^A$, repulsive forces of non-DLVO origin $\mathbf{F}^{ND}$, and contact interactions $\mathbf{F}^C$. The repulsive forces $\mathbf{F}^R$ and $\mathbf{F}^{ND}$ act normally towards the particle center; $\mathbf{F}^R$ decays with interparticle surface separation $h$ over a Debye length $\kappa^{-1}$ as $|\mathbf{F}^R| = F_R \exp[-\kappa(h - 2h_r)]$ for $h > 2h_r$ and $|\mathbf{F}^R| = F_R$ for $h \leqslant 2h_r$. The non-DLVO repulsive forces are dominant when the interparticle gap is comparable to particle surface roughness size [60,61]. So we use a non-DLVO

TABLE I. Simulation parameters.

| $\phi$ | $\dot{\gamma}/\dot{\gamma}_0$ | $\kappa^{-1}$ | $F_A$ | $h_r$ | $F_{ND}$ |
|---|---|---|---|---|---|
| 0.52, 0.57 | 0.001–50.0 | 0.04a | $10^{-3}F_R$ | 0.01a | $10F_R$ |

repulsive force for $h_r \leqslant h \leqslant 2h_r$ with an exponentially decaying form $|\mathbf{F}^{ND}| = F_{ND} \exp[-A(h - h_r)/a]$ for $h \geqslant h_r$ [41] and $|\mathbf{F}^{ND}| = F_{ND}$ for $h < h_r$. We choose $A = 1000$ for this study. Similarly, the attractive force of van der Waals origin also acts normally but in the opposite direction to the repulsive force and is modeled as $|\mathbf{F}^A| = F_A/[(h - h_r)^2 + 0.01]$. Here 0.01 is used to prevent the divergence in $\mathbf{F}^A$ when $h \to h_r$ [2]. We use the DLVO repulsive force as the characteristic force scale to nondimensionalize the governing forces. So the characteristic stress scale is given by $\sigma_0 = F_R/6\pi a^2$ (and rate scale $\dot{\gamma}_0 = \sigma_0/\eta_0$), related to the transition from lubricated contacts (hydrodynamic) where particles are separated to direct contact between particles.

We model the surface roughness as a hemispherical bump of size $h_r$ on the base sphere as shown in the insets in fig. 2. The contact interactions are modeled using the Hertz law for the normal contact force $|\mathbf{F}_n^C| = k_n(\delta/\delta_c)^{3/2}$ and a linear spring for the tangential contact force $\mathbf{F}_t^C = k_t \boldsymbol{\xi}_t$ [1]. Here $\delta = h_r - h$ is the asperity deformation, $\delta_c$ is the threshold for elastic to plastic transition, and $\boldsymbol{\xi}_t$ is the tangential spring stretch. The contact activates only when $h \leqslant h_r$. Contact interactions obey Coulomb's friction law $|\mathbf{F}_t^C| \leqslant \mu \mathbf{F}_n^C$. The details and validation of the algorithm can be found elsewhere [1,45,49]. Figure 2 depicts how $|\mathbf{F}_n| = |\mathbf{F}^R| + |\mathbf{F}^{ND}| - |\mathbf{F}^A| + |\mathbf{F}_n^C|$ varies with $\lambda$. It is well known that $\mu$ is not constant and depends on the normal load $|\mathbf{F}_n^C|$ [5,33,58]. Since $|\mathbf{F}_n^C| \propto \delta^{3/2}$ following the Hertz law, $\mu$ can also be described as a function of the dimensionless interparticle gap $\lambda = h/h_r$ (since $\delta = 1 - \lambda h_r$). We calculate the bulk stress $\boldsymbol{\sigma}$ in the system by volume averaging the stresslets due to all the interactions [1,45,49]. Rheological properties can be quantified from the bulk stress, e.g., the relative viscosity of the suspension $\eta_r = \sigma_{12}/\eta_0\dot{\gamma}$, second normal stress difference $N_2 = \sigma_{22} - \sigma_{33}$. Values of simulation parameters used (unless mentioned otherwise) are summarized in Table I.

*Friction coefficient.* We use the dimensionless gap-size dependent ($\lambda = h/h_r$) Stribeck curve to model $\mu$ [54]. For $\lambda > 1$, the reduction in $\mu$ with decreasing $\lambda$ is captured in lubrication interactions [15] and hence there is no need to use Coulombs friction law explicitly. We approximate $\mu$ in the partial EHL regime by a step function [15] for simplicity. For $\lambda \leqslant 1$, asperities come into contact, resulting in a sudden rise in $\mu$; $\mu$ has a high value if the contact is elastic, i.e., $\delta \leqslant \delta_c$, where $\delta$ is the asperity deformation defined as $\delta = |h - h_r|$ [47,58]. If the asperities deform further such that $\delta > \delta_c$, the contacts transition into the plastic regime, resulting in a steep decrease in $\mu$. Experimental measurements [5] have shown that the friction coefficient decreases with the normal load as $\mu = -a'\ln(|\mathbf{F}_n^C|) + b'$, or in terms of $\lambda$ [since $|\mathbf{F}_n^C| \propto \delta^{3/2}$ by the Hertz law and $\delta = h_r(1 - \lambda)$] we can say $\mu = -a\ln[(1 - \lambda)] + b$ for $0 < \lambda < 1$, where $a'$, $b'$, $a$, and $b$ are constants. We choose $a = \frac{1}{2}$ and $b = -0.2$ in this study. We call this friction model logarithmic decay friction. Data
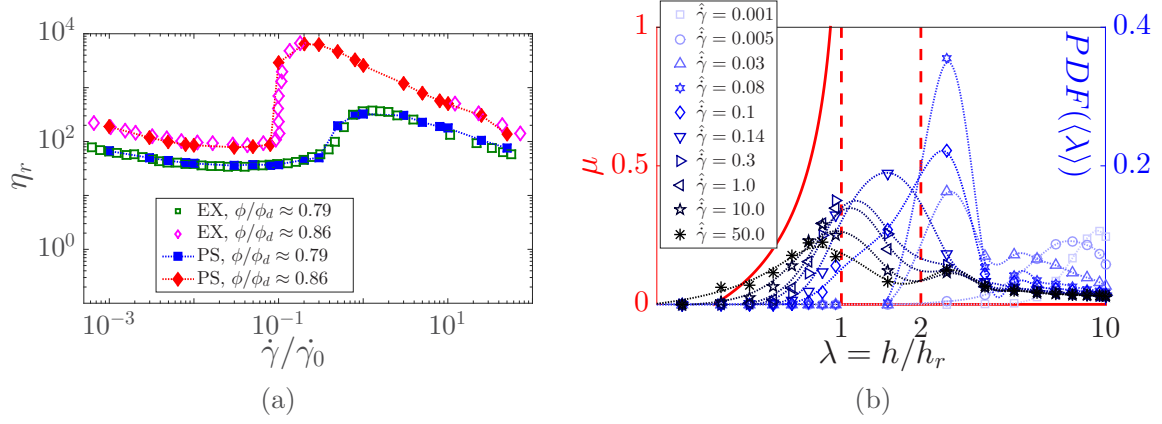
FIG. 3. (a) Relative viscosity as a function of dimensionless shear rate $\dot\gamma/\dot\gamma_0$ for two different volume fractions (PS denotes present simulations) compared against experiments (EX denotes experiments, $\dot\gamma_0 = 200$ s$^{-1}$ for experimental data) of Chatté *et al.* [5]. The volume fractions are scaled with dry close packing fraction $\phi_d$ for direct comparison. For the simulations $\phi_d = 0.66$. (b) Probability distribution function (dotted lines) of the average dimensionless interparticle gap $\langle\lambda\rangle$ with increasing $\hat{\dot\gamma} = \dot\gamma/\dot\gamma_0$ (legend) along with the friction coefficient (solid lines) for the logarithmic decay friction model. Dotted lines are spline fits to guide the eye. Dashed lines demarcate the transition between interaction ranges as explained in Fig. 2.

for additional friction models along with results for varying $a$ and $b$ in the logarithmic decay model are shown in Sec. V.

Thus, all the expressions used for various forces have a solid experimental backing. One way to distinguish them experimentally is to measure them carefully in terms of the interparticle gaps as modeled in the paper. We have used the expressions from the experimental measurements [5] to make a quantitative comparison with their results. However, the freedom to choose the values of various input parameters such as the relative magnitudes of the forces, the Debye length, parameters $a$ and $b$ in the friction law, and the roughness size based on the system enables the model to capture various regimes in the flow diagram. For the systems which do not show a Newtonian plateau, one only needs to switch off the non-DLVO forces or make their magnitude 0. This allows us to unify various flow regimes observed for non-Brownian suspensions as demonstrated in the following sections.

## IV. RESULTS AND DISCUSSION

We demonstrate the accuracy of the proposed model by direct comparison of the calculated suspension relative viscosity with experimental values for polyvinyl chloride particles suspended in a Newtonian fluid medium [5] in Fig. 3(a). Chatté *et al.* [5] used a system that had previously been characterized to take advantage of the data from the literature. They used a suspension of polyvinyl chloride (PVC) particles suspended in a Newtonian fluid (1,2-cyclohexane dicarboxylic acid diisononyl ester). The classical studies by Hoffman [4,9] also used PVC particles. In addition, PVC particles are known to transition from a lubricated to a frictional contact regime [33]. They used two suspensions with a log-normal distribution (D1) and a trimodal distribution with log-normal peaks (D2). The sizes of the particles are chosen in such a way that the Brownian effects are negligible. Hence, these suspensions are non-Brownian.

It has been shown that a polydisperse system with a log-normal distribution of the particle sizes can be quantitatively

modeled as a bidisperse system in a way such that both of these suspensions have similar rheological property values [62]. Hence, we are particularly interested in the D1 suspension as we can use a simple bidisperse system and still reproduce the same rheology as done herein. However, because these two systems have different random packing fractions $\phi_d$, in order to compare the viscosities, we need to normalize the volume fraction values for these systems by $\phi_d$ [8]. The random packing fraction for D1 suspension is approximately 69%, while the random packing fraction for the bidisperse system used for simulations is approximately 67%. Hence, close quantitative agreement between the experiments and simulations is expected if we accurately model the underlying physics. Also note that to access such a wide range of shear rate values and the different regimes in the flow curve of these suspensions, they used a combination of rotational and special capillary rheometers as simple rotational rheometers cannot access regions of very high normal stress differences [28,36]. These regions correspond to high viscosity values after the shear thickening transition and the second shear thinning regime.

Figure 3(a) shows that the proposed model does an excellent job in quantitatively capturing the rate-dependent rheological properties in low, intermediate, and high shear rate limits. This shows that the hypothesis that accounting for non-DLVO interactions recovers the initial transition from shear thinning to the intermediate Newtonian regime. A universal friction law based on the Stribeck curve accurately recovers the onset of ST and then the second shear thinning that is typical of dense non-Brownian suspensions is indeed true.

We plot the probability distribution function (PDF) of the ensemble average of the dimensionless interparticle gap $\langle\lambda\rangle$ at different shear rate values corresponding to different regimes in the rheological state diagram [Fig. 3(b)] to explain the observed shear-rate-dependent rheological behavior. With increasing shear rate values, the peak and mean of the PDF of $\langle\lambda\rangle$ shift to the left on the Stribeck curve. This determines the various transitions in the rheological state diagram. At

low shear rates, the particles are prevented from coming into direct contact due to the combined effect of the repulsive and attractive forces of DLVO origin. This is analogous to having particles with bigger radii. As we increase the shear rate, the particles are pushed closer, resulting in the reduction of this apparent bigger radius. As a result, the effective volume fraction of the suspension decreases with increasing shear rate in this regime, which results in the observed shear thinning. In the intermediate shear rate regime, the stress is high enough to overcome the DLVO repulsive barrier between the particles so that the particles are on average separated by a distance approximately $O(h_r)$. However, the stress is not high enough to overcome the short-range non-DLVO repulsion, which is an order of magnitude higher than the DLVO barrier. This leads to the Newtonian plateau in the relative viscosity. This plateau in the $\eta_r$ at intermediate $\dot{\gamma}$ values is not present if we do not consider short-range repulsive forces of non-DLVO origins [2] as shown in Sec. V B. This indicates the governing role of non-DLVO forces in dense non-Brownian suspensions.

If we increase the shear rate further, the stress in the suspension becomes high enough so that the repulsive barrier due to the DLVO and non-DLVO forces breaks and the particles come into contact due to the touching of asperities on their surfaces. The contact remains in the elastic region, resulting in a high $\mu$ between the particles and constraints on the relative sliding between the particles. This leads to a jump in the suspension viscosity. The shear thickening transition takes place above a critical shear rate value $\dot{\gamma}_c$ (e.g., $\dot{\gamma}_c/\dot{\gamma}_0$ for $\phi/\phi_{RCP} \approx 0.86$ is 0.1). In the shear thickening transition regime, the viscosity increases gradually (continuous shear thickening) at lower volume fractions, while it undergoes a sudden increase (discontinuous shear thickening) at higher volume fractions. As we increase the shear rate further, the asperities are plastically deformed ($\delta > \delta_c$). As a result, the coefficient of friction between the particles decreases significantly, which is analogous to relaxation of the constraint on the relative sliding motion between the particles. This gives rise to the second shear thinning transition at high shear rates. The consequences of this shift in the PDF of $\langle \lambda \rangle$ to the left with increasing $\dot{\gamma}$ on the transitions in dominant interaction between the particles and the suspension rheology are depicted pictorially in Fig. 4.

The shift in the PDF of $\langle \lambda \rangle$ manifests itself in determining the relative magnitudes of different contributions from hydrodynamic ($\eta_r^H$), noncontact ($\eta_r^{NC}$) (DLVO and non-DLVO), and contact ($\eta_r^C$) interactions to the total relative viscosity ($\eta_r$) in Fig. 5(b). As we increase the shear rate, $\eta_r^H$ increases gradually. At low and intermediate shear rate values, $\eta_r^C$ is 0 as the repulsive barrier prevents direct contacts. In this regime, $\eta_r^{NC}$ decreases with increasing shear rate, which explains the first shear thinning behavior. However, beyond $\dot{\gamma}_c$ the particles come into direct contact, thus resulting in the sudden jump in $\eta_r$ due to high $\eta_r^C$. This is also known as a lubricated-frictional transition, which has been well studied [63]. In the high shear rate regime beyond $\dot{\gamma}_c$, the contribution from the contact interactions to the bulk suspension stress is dominant and hence determines the suspension viscosity. Since $\mu$ decreases with increasing shear rate due to the lowering of $\lambda$, $\eta_r^C$, and as a consequence $\eta_r$, decreases with an increase in the shear rate.
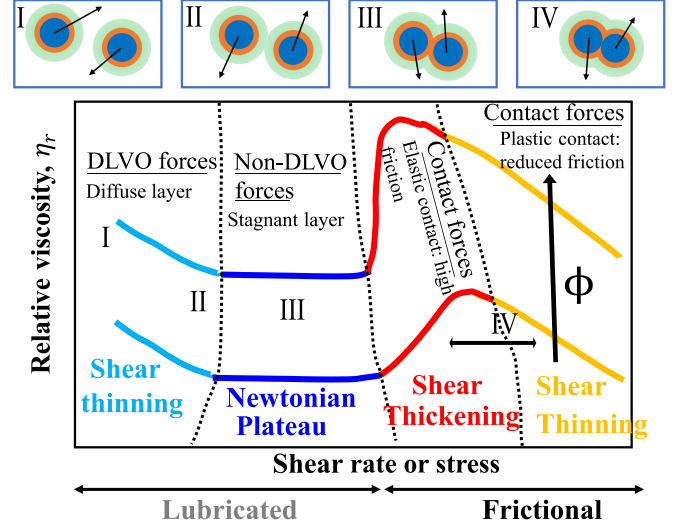


FIG. 4. Scheme of the physics involved in the shear thinning (I and II), Newtonian plateau (III), and shear thickening–shear thinning (IV) regimes in the rheological behavior of a typical dense non-Brownian suspension. The insets at the top show the approximate interparticle gaps in regimes I–IV. In these insets, the outermost circle represents the range of DLVO forces, the inner orange circle represents the range in which non-DLVO forces are dominant, and the innermost circle represents the particles. Thus, with increasing shear rate we observe different regimes depending on which forces are dominant in the suspension on average as depicted by the overlaps of different force zones in the insets.

The neutron scattering [22] and rheoconfocal [64] measurements for Brownian suspensions [Pe $< O(10^5)$] hint at the role of ordering in the colloids in the initial shear thinning. Since we use a bidisperse suspension for preventing any clustering and ordering in the suspension, we expect the particles to remain homogeneously distributed. Still, to investigate if there is any ordering in the suspensions, we evaluate the ordering metric $Q_6$ [65] to quantify the ordering in the suspensions; $Q_6$ can be calculated as

$$Q_6 = \sqrt{\frac{4\pi}{13} \sum_{m=-6}^{m=6} \langle Y_{6m} \rangle^2}. \tag{1}$$

Here $Y_{nm}(\theta, \phi)$ are the spherical harmonics which depend on the polar ($\theta$) and the azimuthal ($\phi$) angles, which together give us the orientation of the center-to-center vector for the neighboring particle pairs. In addition, $\langle Y_{6m} \rangle$ is the average of $Y_{6m}(\theta, \phi)$ over all the neighboring particles in the suspension. Further, $Q_6$ quantifies the ordering in the suspension system; $Q_6 = 0$ indicates a completely homogeneous or disordered system. The maximum value that $Q_6$ can have is approximately equal to 0.575. This maximum values is reached for a face-centered-cubic structure.

We plot the order metric $Q_6$ in Fig. 5(b). A small value of $Q_6$ signifies the absence of ordering in the suspension, while a large value (greater than 0.5) indicates a strong ordering. We find that $Q_6$ values are negligible, which indicates the absence of any ordering. However, we observe a gradual rise and a spike in $Q_6$ for the lower shear rates just before the ST transition (the end of Newtonian plateau). The value of $Q_6$
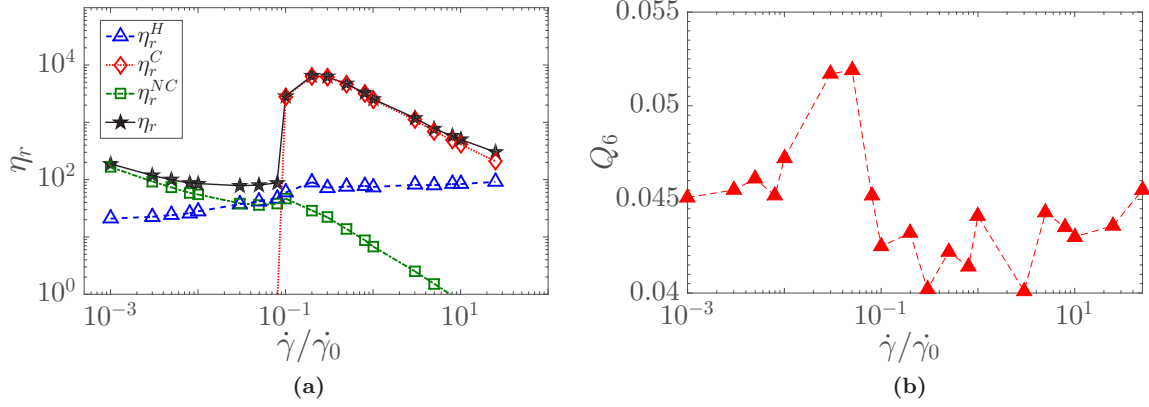
FIG. 5. (a) Contributions from hydrodynamic ($\eta_r^H$), noncontact ($\eta_r^{NC}$) (DLVO and non-DLVO), and contact ($\eta_r^C$) interactions to the total relative viscosity of the suspension for $\phi/\phi_d \approx 0.86$. The trends in the respective contribution follow from Fig. 4. Lines are for guiding the eye. (b) Flow curve for different coefficient of friction functions for $\phi/\phi_d \approx 0.86$.

drops down significantly once the suspension undergoes a ST transition ($\dot{\gamma}/\dot{\gamma}_0 \approx 0.1$). These calculations insinuate that the ordering in the initial thinning regime for monodisperse suspensions might be the consequence of DLVO and non-DLVO forces preventing the particles from coming into hard contacts as the peak in $Q_6$ coincides with the range of shear rates when DLVO and non-DLVO interactions are dominant.

## V. PREDICTING OTHER FLOW CURVES

We have used the expressions for DLVO repulsive force and the coefficient of friction from the experimental measurements by Chatté et al. [5] to make a quantitative comparison with their results and validate the model. However, the freedom to choose the values of various input parameters such as the relative magnitudes of the forces, the Debye length, the friction law, and the roughness size based on the system one is trying to model enables the model to capture various regimes and transitions in the flow diagram. Increasing the magnitude of attractive forces or increasing the Debye length results in a steeper initial thinning [2,66] (Sec. V A). Decreasing (increasing) the magnitude of non-DLVO forces will result in a narrower (wider) Newtonian plateau (Sec. V B). For the systems which do not show the second shear thinning, one only needs to make the coefficient of friction a constant, which gives us a constant viscosity in the shear thickened regime [45] (Sec. V C). Though simulation results show that only constraining the sliding motion between the particles gives satisfactory agreement with experimental data for smooth particle suspensions [47], our model can also account for roughness effects (Sec. V D) both geometrically (by varying the roughness size [45]) and physically (by constraining the rolling and twisting motion [67]). Other constraints on the particle motion such as rolling and twisting friction become important only for rough particles [32]. Incorporating rolling and twisting friction in the current model is straightforward but not done as we are dealing with smooth particle suspensions. This makes the proposed model very general and applicable to a wide variety of systems.

In this section we present the simulation results obtained by varying various controlling parameters in the proposed model. The key parameters in the model are (i) the DLVO repulsive force scale $F_R$, (ii) the DLVO attractive force scale $F_A$, (iii) the non-DLVO short-range repulsive force scale $F_{ND}$, and (iv) the exact dependence of the coefficient of friction on the contact normal load $|\mathbf{F}_c^N|$ or on the asperity deformation $\delta$. Each of these parameters determines the suspension behavior and the critical transition shear rates for the four regimes described.

### A. Magnitude of $F_A$ controls the initial shear thinning

We first plot the DLVO force profiles for an increase in the magnitude of the attractive forces $F_A$ in the DLVO interactions. These are presented in Fig. 6(a). For these simulations, we keep the other parameters fixed as given in Table I. We use the same friction model as described herein. We vary only the magnitude of the attractive forces $F_A$. Figure 6(b) shows the effect of changing the magnitude of the attractive forces in the DLVO interactions. As expected, with an increase in the magnitude of the attractive forces, we observe that the slope of the shear thinning curve at low shear rate values increases [2]. With the increase in $F_A$, the $\lambda$ below which the net DLVO force is repulsive decreases. Note that the critical shear rate for shear thickening transition does not change with changing $F_A$. This is because, before the lubricated-to-frictional transition can take place, the particles still need to overcome the non-DLVO repulsive forces. So, in this model, the magnitude of the non-DLVO forces determines the critical shear rate for the onset of the shear thickening transition. The Newtonian plateau disappears in the absence of non-DLVO forces. Thus, we can reproduce the thinning-thickening-thinning transition using the proposed model as well. Changing the magnitude of the non-DLVO forces does not change the viscosity jump magnitude and the viscosities in the second shear thinning regime. This is because both of these depend on the friction model used.

### B. $F_{ND}$ controls the presence, absence, and range of the intermediate Newtonian plateau

Figure 7(a) shows the effect of varying the magnitude of the non-DLVO forces on the flow curve of dense non-Brownian suspensions. For these simulations, we keep the other parameters fixed as given in Table I and change only
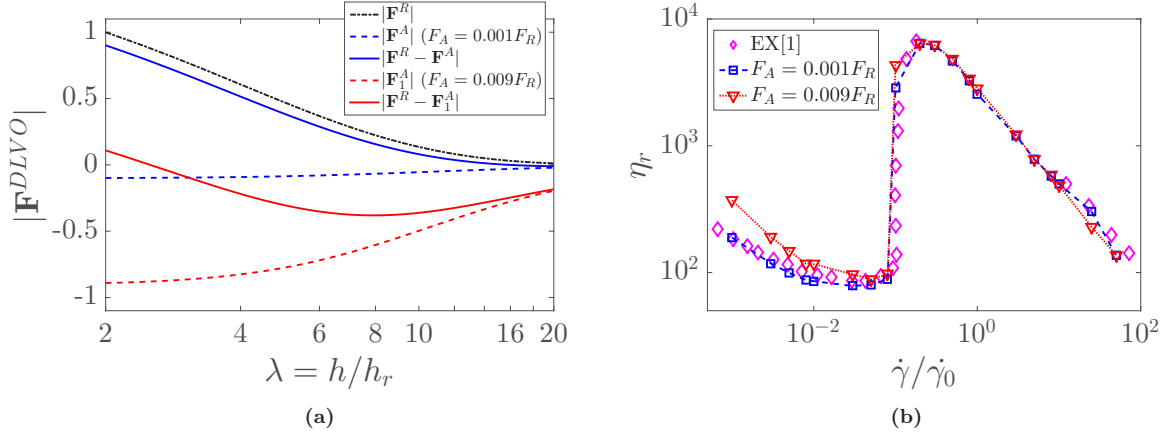
FIG. 6. (a) DLVO force (repulsion and attraction) profiles as a function of dimensionless gap for two different attractive force magnitudes. (b) Effect of varying the attractive force magnitude on the first shear thinning regime.

$F_{ND}$. We use the same friction model as before. We only vary the magnitude of the non-DLVO forces. The range of shear rates over which the Newtonian plateau is observed increases with an increase in the magnitude of the non-DLVO forces. This is because non-DLVO forces are essentially noncontact forces. So as their magnitude increases, the lubricated-to-frictional transition in the particle contacts is pushed to higher critical shear rates. Changing the magnitude of the non-DLVO forces, however, does not change the slope of the second shear thinning curve at high shear rates as it depends on the friction model. This investigation shows that the presence or absence and the range of the Newtonian plateau is determined by the presence or absence and the magnitude of the non-DLVO interactions, respectively. More experiments measuring the non-DLVO forces between particles made of different materials and their corresponding Newtonian plateau range can shed more light on the role of the non-DLVO interactions.

The effect of changing the magnitude of non-DLVO interactions on the ordering parameter $Q_6$ is presented in Fig. 7(b). As we use a bidisperse system, we observe only a weak ordering in the suspensions. Previous studies in the colloidal regime [22,64] have attributed the shear thinning at low shear rates to the ordering of particles in layers in the colloids. In our simulations for non-Brownian systems, there is no evidence of any significant ordering. Hence, the initial shear thinning regime observed is due to the apparent lowering of the volume fraction as the interparticle gaps between the particles decrease as we increase the shear rate. The particles are pushed closer as the hydrodynamic force dominates over the noncontact DLVO forces with an increase in the shear rate. We however see a gradual rise in $Q_6$ until it reaches a peak just before the shear thickening transition as shown in Fig. 7(b). The peak is sustained over the range for which we observe the Newtonian plateau. This hints that the ordering and the flattening of the viscosity just before the shear thickening might be the outcomes of the noncontact interactions between the particles. Experiments can shed more light on this link.

## C. Governing role of friction in the ST transition and rheology at high shear rates

The second shear thinning after the shear thickening transition at high shear rates is the result of the decreasing coefficient of friction in the boundary contact regime of the
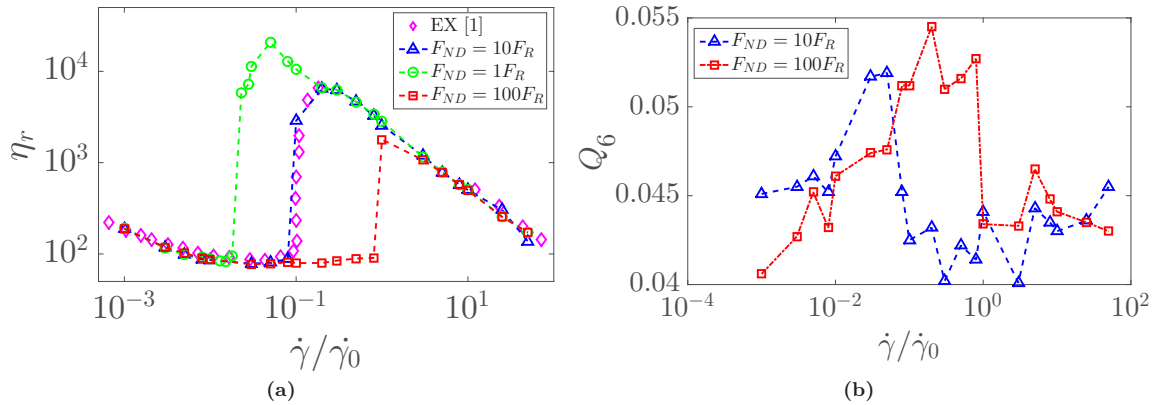


FIG. 7. (a) Effect of changing the magnitude of the non-DLVO force. The Newtonian plateau disappears in the absence of non-DLVO forces. Thus, we can reproduce the thinning-thickening-thinning transition using the proposed model as well. This is useful for suspensions which do not have a significant Newtonian plateau, e.g., silica particles [22]. (b) Order metric $Q_6$ for two different non-DLVO force magnitude. The gradual increase in $Q_6$ in the first shear thinning regime and peak in the Newtonian regime hint at the link between ordering and the initial shear thinning Newtonian plateau [22].
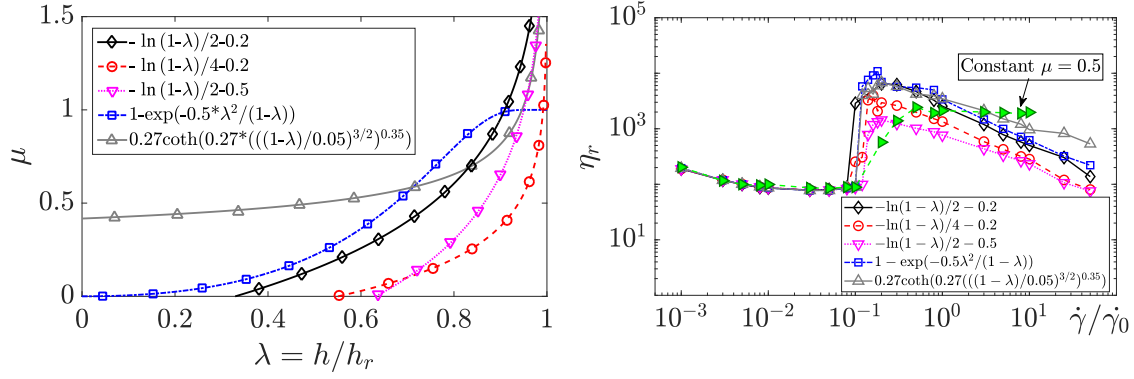
FIG. 8. (a) Different friction laws tested for the sensitivity analysis of the model to $\mu$. Here $-a\ln(1-\lambda)+b$ is the logarithmic decay model derived from the experimental measurements from Ref. [5]. The black solid line ($a=\frac{1}{2}$ and $b=-0.2$), red dashed line ($a=\frac{1}{4}$ and $b=-0.2$), and pink dotted line ($a=\frac{1}{2}$ and $b=-0.5$) show how $\mu$ for the logarithmic decay model changes with dimensionless interparticle gap $\lambda = h/h_r = 1 + \delta/h_r$. The blue dash-dotted line shows a hypothetical exponentially decaying $\mu$. Finally, the gray solid line shows the model of Brizmer $et\ al.$ [58] for $\mu$ which has been previously used in the literature to explain the shear thinning in dense non-Brownian suspensions [47]. (b) Variation of viscosity for different friction models. If we use a constant $\mu$ instead, we will not observe the second shear thinning regime. The data show that the friction model determines the viscosity jump during the shear thickening transition and the slope in the second shear thinning regime. The flow curve for suspensions which do not exhibit the second shear thinning can be obtained by choosing a constant coefficient of friction.

Stribeck curve. Hence, the viscosity jump across the shear thickening transition and the slope of the second shear thickening regime are determined by the friction law used in the model. This is depicted in Fig. 8(b) for friction laws shown in Fig. 8(a). A higher value of friction leads to a larger viscosity. Hence, the model of Brizmer $et\ al.$ has a larger viscosity in the second shear thinning regime than other friction laws. A friction law with a less steep decrease with particle deformation (e.g., the law of Brizmer $et\ al.$) results in a less steep second shear thinning regime. A constant $\mu$ will result in the disappearance of the second shear regime [45] [see Fig. 8(b)].

There is an ongoing debate in the community regarding the presence of the second shear thinning regime as it is not observed in all the systems. We would like to point out that the second shear thinning has been observed to be prominent for high volume fractions and has been seen to be present at very high shear rates (greater than $10^4$–$10^5$ s$^{-1}$). Hence, to observe this regime, one would need to be able to shear the suspension at such high shear rates. Most of the experimental studies on ST suspensions do not explore such a high shear rate regime as they stop their investigation right after the suspension undergoes ST [22,29–31,36,68–70]; however, those which do, have reported the second shear thinning at high shear rates in suspensions [4,5,9,28]. In addition, we expect the second shear thinning to depend on the particle material as well. Since the asperities need be deformed plastically to enter the low coefficient of friction region, the stress (and hence shear rate) required for the same would depend on particle properties. For example, since the Young and elastic moduli of silica particles are larger than PVC particles, a significantly higher shear stress or rate would be required to deform silica asperities plastically, thus delaying the onset of second shear thinning to very high $\dot{\gamma}$ values. We expect our simulation results to encourage experimentalists to investigate different suspension systems at very high shear rate values to shed more light on the link between plastic deformation of particle asperities and the second shear thinning regime.

### D. Effect of particle surface roughness

Earlier theoretical and numerical studies had predicted that increasing the particle surface roughness would lead to a decrease in the suspension viscosity [71]. However, recent experiments show that rough particle suspensions have a higher viscosity compared to smooth particle suspensions [52]. We have resolved this discrepancy and showed that the increase in suspension viscosity with particle surface roughness can be explained by using a normal load or roughness deformation-dependent $\mu$ [1] similar to the one used in this study.

The proposed model in this study is equipped to quantify the effects of varying particle roughness which is not possible in models which allow particle overlaps. Simulation
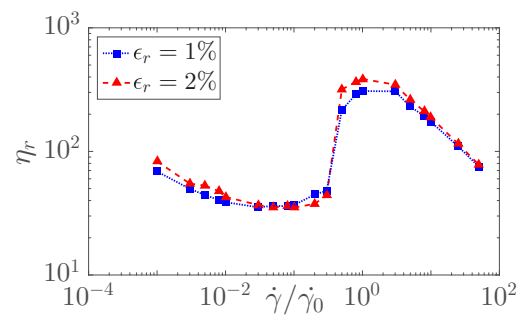


FIG. 9. Effect of varying particle surface roughness height $\epsilon_r$ on the suspension viscosity. Increasing surface roughness results in a stronger initial shear thinning and increases the viscosity during and beyond the ST transition. Note that the ST transition is governed by the direct contact between the particles which is due to the breaking of the lubrication film due to the particle asperities. Here all the other parameters are the same as given in Table I, except $\epsilon_r$, which is varied. Here $\phi = 52\%$. The increase in the viscosity with roughness in the thinning regimes is consistent with Ref. [52] and the increase in the viscosity during the ST jump is consistent with Ref. [72]. The viscosities in the Newtonian plateau are comparable for small change in the roughness values.
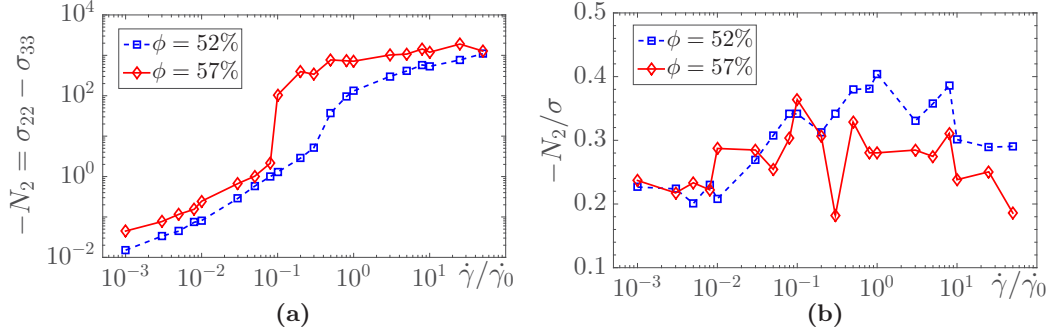
FIG. 10. (a) Evolution of second normal stress difference $N_2$ with applied dimensionless shear rate; $N_2$ is always negative. (b) $N_2$ scaled by the shear stress in the suspension. This plot shows that $N_2$ mimics the stress in the system.

results accurately predict a rise in the suspension viscosity with particle asperity size $\epsilon_r$, as shown in Fig. 9. The increase in the suspension viscosity with particle roughness manifests itself in the form of a higher viscosity jump across the ST transition, in agreement with previous experiments [72] and simulations [45].

## VI. NORMAL STRESS DIFFERENCES

Figures 10(a) and 10(b) show the dependence of the second normal stress difference $N_2 = \sigma_{22} - \sigma_{33}$ and the dimensionless normal stress difference $N_2/\sigma_{12}$ in the dimensionless shear rate. We observe $N_2$ to be negative for all the investigated input parameters. We find that $N_2$ qualitatively mimics the shear stress $\sigma$ in the suspension. We also find that the first normal stress difference is small compared to $N_2$ and is dominated by fluctuations. Hence, it is not presented here.

## VII. CONCLUSION

We propose a universal model which can quantitatively predict all of the four regimes, viz., shear thinning, Newtonian plateau, shear thickening, and shear thinning and the transition from one regime to the other with increasing shear rate or stress typical to the flow behavior of dense non-Brownian suspensions. Thus, unifying disparate rate-dependent rheological regimes in the flow curve of a dense non-Brownian suspension of smooth particles. The unifying mechanism is based on the competition between the interparticle hydrodynamic interactions, nonhydrodynamic interactions of DLVO and non-DLVO origins, contact forces, and a Stribeck curve for the friction coefficient (a constraint mechanism), each interaction resulting in a characteristic stress scale in the system. The switching between the dominant stress scale with increasing shear rate or stress explains the various regimes and transitions observed in a dense non-Brownian suspension [particle sizes greater than $O(1 \ \mu\text{m})$]. Specifically, we showed that accounting for the non-DLVO forces and a coefficient of friction decreasing with the increasing normal load (asperity deformation) is crucial to quantitatively reproduce the intermediate Newtonian plateau and the second shear thinning in the same framework. We validated the proposed hypothesis by performing particle-scale dynamic simulations and compared the results with previous experiments.

The presence of a Newtonian plateau [5,7] was explained by the inclusion of non-DLVO interactions that are noncon-

tact interactions [41] and delay the onset of the lubricated to frictional transition (hence ST). Furthermore, we did not find any significant ordering in the initial shear thinning regime as it was observed in some cases for monodisperse suspensions. This begets an interesting question whether the ordering at low shear rates or stresses for monodisperse suspensions is an outcome of various noncontact interactions rather than being the reason for the initial shear thinning? Further investigations are needed in this direction.

The results also show that only constraining the sliding motion between the particles is enough for smooth particle suspensions, unlike rough particles where constraint on rolling motion might be crucial [32]. The ST transition is the result of constraints on the relative particle motions due to friction, while the second shear thinning arises due to the reduction in the coefficient of friction with asperity deformation (or normal load) at a very high shear rate or stress. Our simulation results show that using experimentally obtained expressions for the nonhydrodynamic interactions and the constraint mechanism (e.g., coefficient of friction) is required to obtain quantitative agreement with the experimental results.

Although we have used specific force profiles from the direct measurements [5] for DLVO forces and $\mu$, the model can reproduce the flow curve for any generic system given its repulsive, attractive, non-DLVO force profiles, and friction law. We demonstrated the versatility of the proposed model to reproduce a gamut of flow behaviors by varying the relative magnitudes and expressions of various interactions. In addition, the model accurately predicts a rise in the suspension viscosity with particle surface roughness, in agreement with recent experiments. These results show that the macroscopic rheological behavior is determined by the microscopic particle-pair interactions. It would also be interesting to investigate the effects of other collision models [73,74]. Thus, to gain further insight into the physics behind the rheological behavior of dense suspensions, accurate measurements of interparticle interactions (especially non-DLVO interactions) and $\mu$ as a function of interparticle gap while immersed in the fluid medium are needed.

[1] R. V. More and A. M. Ardekani, J. Rheol. **64**, 67 (2019).
[2] A. Singh, S. Pednekar, J. Chun, M. M. Denn, and J. F. Morris, Phys. Rev. Lett. **122**, 098004 (2019).
[3] I. E. Zarraga and D. T. Leighton, Phys. Fluids **13**, 565 (2001).
[4] R. Hoffman, Trans. Soc. Rheol. **16**, 155 (1972).
[5] G. Chatté, J. Comtet, A. Niguès, L. Bocquet, A. Siria, G. Ducouret, F. Lequeux, N. Lenoir, G. Ovarlez, and A. Colin, Soft Matter **14**, 879 (2018).
[6] P. Pham, B. Metzger, and J. E. Butler, Phys. Fluids **27**, 051701 (2015).
[7] J. J. Stickel and R. L. Powell, Annu. Rev. Fluid Mech. **37**, 129 (2005).
[8] É. Guazzelli and O. Pouliquen, J. Fluid Mech. **852**, 1 (2018).
[9] R. Hoffman, J. Colloid Interf. Sci. **46**, 491 (1974).
[10] E. Brown and H. M. Jaeger, Phys. Rev. Lett. **103**, 086001 (2009).
[11] R. Mari, R. Seto, J. F. Morris, and M. M. Denn, J. Rheol. **58**, 1693 (2014).
[12] B. M. Guy, J. A. Richards, D. J. M. Hodgson, E. Blanco, and W. C. K. Poon, Phys. Rev. Lett. **121**, 128001 (2018).
[13] J. F. Brady and G. Bossis, J. Fluid Mech. **155**, 105 (1985).
[14] J. R. Melrose and R. C. Ball, J. Rheol. **48**, 937 (2004).
[15] N. Fernandez, R. Mani, D. Rinaldi, D. Kadau, M. Mosquet, H. Lombois-Burger, J. Cayer-Barrioz, H. J. Herrmann, N. D. Spencer, and L. Isa, Phys. Rev. Lett. **111**, 108301 (2013).
[16] S. Jamali and J. F. Brady, Phys. Rev. Lett. **123**, 138002 (2019).
[17] E. da C Andrade and J. Fox, Proc. Phys. Soc. B **62**, 483 (1949).
[18] A. Metzner and M. Whitlock, Trans. Soc. Rheol. **2**, 239 (1958).
[19] R. L. Hoffman, Adv. Colloid Interf. Sci. **17**, 161 (1982).
[20] J. F. Brady and J. F. Morris, J. Fluid Mech. **348**, 103 (1997).
[21] N. J. Wagner and J. F. Brady, Phys. Today **62** (10), 27 (2009).
[22] D. Kalman and N. Wagner, Rheol. Acta **48**, 897 (2009).
[23] D. Lootens, H. van Damme, Y. Hémar, and P. Hébraud, Phys. Rev. Lett. **95**, 268302 (2005).
[24] E. Brown and H. M. Jaeger, Rep. Prog. Phys. **77**, 046602 (2014).
[25] J. F. Brady and G. Bossis, Annu. Rev. Fluid Mech. **20**, 111 (1988).
[26] T. N. Phung, J. F. Brady, and G. Bossis, J. Fluid Mech. **313**, 181 (1996).
[27] J. F. Brady and D. R. Foss, J. Fluid Mech. **407**, 167 (2000).
[28] E. Brown and H. Jaeger, J. Rheol. **56**, 875 (2012).
[29] H. Laun, J. Non-Newtonian Fluid Mech. **54**, 87 (1994).
[30] J. R. Royer, D. L. Blair, and S. D. Hudson, Phys. Rev. Lett. **116**, 188301 (2016).
[31] B. M. Guy, M. Hermes, and W. C. K. Poon, Phys. Rev. Lett. **115**, 088304 (2015).
[32] A. Singh, C. Ness, R. Seto, J. J. de Pablo, and H. M. Jaeger, Phys. Rev. Lett. **124**, 248005 (2020).
[33] J. Comtet, G. Chatté, A. Niguès, L. Bocquet, A. Siria, and A. Colin, Nat. Commun. **8**, 15633 (2017).
[34] M. Wyart and M. E. Cates, Phys. Rev. Lett. **112**, 098302 (2014).
[35] N. Nakajima and E. Harrell, J. Elastom. Plast. **41**, 277 (2009).
[36] D. P. Kalman, B. A. Rosen, and N. J. Wagner, in *Proceedings of the XV International Congress on Rheology: The Society of Rheology 80th Annual Meeting, Monterey, 2008*, edited by A. Co, G. L. Leal, R. H. Colby, and A. J. Giacomin, AIP Conf. Proc. No. 1027 (AIP, Melville, 2008), pp. 1408–1410.
[37] A. Vázquez-Quesada, R. I. Tanner, and M. Ellero, Phys. Rev. Lett. **117**, 108001 (2016).
[38] A. Fall, A. Lemaitre, F. Bertrand, D. Bonn, and G. Ovarlez, Phys. Rev. Lett. **105**, 268303 (2010).
[39] N. Y. C. Lin, B. M. Guy, M. Hermes, C. Ness, J. Sun, W. C. K. Poon, and I. Cohen, Phys. Rev. Lett. **115**, 228304 (2015).
[40] J. N. Israelachvili, *Intermolecular and Surface Forces* (Academic, New York, 2011).
[41] I. Szilagyi, G. Trefalt, A. Tiraferri, P. Maroni, and M. Borkovec, Soft Matter **10**, 2479 (2014).
[42] P. Richmond, J. Chem. Soc. Faraday Trans. 2 **70**, 1066 (1974).
[43] Richmond, J. Chem. Soc., Faraday Trans. 2 **71**, 1154 (1975).
[44] S. J. Miklavic, D. Y. Chan, L. R. White, and T. W. Healy, J. Phys. Chem. **98**, 9022 (1994).
[45] R. More and A. Ardekani, J. Rheol. **64**, 283 (2020).
[46] C. Clavaud, A. Bérut, B. Metzger, and Y. Forterre, Proc. Natl. Acad. Sci. USA **114**, 5147 (2017).
[47] L. Lobry, E. Lemaire, F. Blanc, S. Gallier, and F. Peters, J. Fluid Mech. **860**, 682 (2019).
[48] A. Singh, R. Mari, M. M. Denn, and J. F. Morris, J. Rheol. **62**, 457 (2018).
[49] R. More and A. Ardekani, J. Rheol. **64**, 1107 (2020).
[50] R. G. Bayer, *Mechanical Wear Prediction and Prevention* (Dekker, New York, 1994).
[51] M. M. Maru and D. K. Tanaka, J. Braz. Soc. Mech. Sci. Eng. **29**, 55 (2007).
[52] R. I. Tanner and S. Dai, J. Rheol. **60**, 809 (2016).
[53] I. Hutchings and P. Shipway, *Tribology: Friction and Wear of Engineering Materials* (Butterworth-Heinemann, Oxford, 2017).
[54] M. J. Neale, *The Tribology Handbook* (Elsevier, Amsterdam, 1995).
[55] J. J. Adler, Y. I. Rabinovich, and B. M. Moudgil, J. Colloid Interf. Sci. **237**, 249 (2001).
[56] H. Kamiya, K. Gotoh, M. Shimada, T. Uchikoshi, Y. Otani, M. Fuji, S. Matsusaka, T. Matsuyama, J. Tatami, K. Higashitani, K. Kurihara, N. Ishida, M. Suzuki, H. Abe, Y. Otsubo, and M. Miyahara, in *Nanoparticle Technology Handbook*, edited by M. Naito, M. Hosokawa, T. Yokoyama, and K. Nogi (Elsevier, Amsterdam, 2008), pp. 113–176.
[57] Y. Diao and R. M. Espinosa-Marzal, Proc. Natl. Acad. Sci. USA **113**, 12047 (2016).
[58] V. Brizmer, Y. Kligerman, and I. Etsion, Tribol. Lett. **25**, 61 (2007).
[59] R. C. Ball and J. R. Melrose, Physica A **247**, 444 (1997).
[60] D. F. Parsons, R. B. Walsh, and V. S. Craig, J. Chem. Phys. **140**, 164701 (2014).

[61] N. Eom, D. F. Parsons, and V. S. Craig, J. Phys. Chem. B **121**, 6442 (2017).

[62] S. Pednekar, J. Chun, and J. F. Morris, J. Rheol. **62**, 513 (2018).

[63] J. F. Morris, Phys. Rev. Fluids **3**, 110508 (2018).

[64] M. Ramaswamy, N. Y. C. Lin, B. D. Leahy, C. Ness, A. M. Fiore, J. W. Swan, and I. Cohen, Phys. Rev. X **7**, 041005 (2017).

[65] M. Rintoul and S. Torquato, J. Chem. Phys. **105**, 9258 (1996).

[66] R. Mari, R. Seto, J. F. Morris, and M. M. Denn, Proc. Natl. Acad. Sci. USA **112**, 15326 (2015).

[67] A. Singh and P. R. Nott, J. Fluid Mech. **412**, 279 (2000).

[68] W. H. Boersma, J. Laven, and H. N. Stein, AIChE J. **36**, 321 (1990).

[69] Y. S. Lee and N. J. Wagner, Ind. Eng. Chem. Res. **45**, 7015 (2006).

[70] M. Lee, M. Alcoutlabi, J. Magda, C. Dibble, M. Solomon, X. Shi, and G. McKenna, J. Rheol. **50**, 293 (2006).

[71] S. Gallier, E. Lemaire, F. Peters, and L. Lobry, J. Fluid Mech. **757**, 514 (2014).

[72] C.-P. Hsu, S. N. Ramakrishna, M. Zanini, N. D. Spencer, and L. Isa, Proc. Natl. Acad. Sci. USA **115**, 5117 (2018).

[73] A. M. Ardekani and R. H. Rangel, Journal of fluid mechanics **596**, 437 (2008).

[74] A. M. Ardekani, D. D. Joseph, D. Dunn-Rankin, and R. H. Rangel, Journal of fluid mechanics **633**, 475 (2009).